On the role of roughness valleys in turbulent Rayleigh-Bénard convection

Mebarek Belkadi, Anne Sergent, Yann Fraigneau, Bérengère Podvin

To cite this version:

Mebarek Belkadi, Anne Sergent, Yann Fraigneau, Bérengère Podvin. On the role of roughness valleys in turbulent Rayleigh-Bénard convection. Journal of Fluid Mechanics, 2021, 923, pp.A6. 10.1017/jfm.2021.583 . hal-03029901v2

On the role of roughness valleys in turbulent Rayleigh-Bénard convection

Mebarek Belkadi[1,2,3], **Anne Sergent**[1,4]†, **Yann Fraigneau**[1] and **Bérengère Podvin**[1]

[1]Université Paris-Saclay, CNRS, LIMSI, F-91400 Orsay, France

[2]Collège doctoral, Sorbonne Université, F-75005 Paris, France

[3]Laboratory of Turbomachinery, Ecole Militaire Polytechnique, Bordj El Bahri, 16111, Algiers, Algeria

[4]Faculté des Sciences et Ingénierie, UFR d'Ingénierie, Sorbonne Université, F-75005 Paris, France

(Received xx; revised xx; accepted xx) version: 13 December 2020

Three-dimensional direct numerical simulations are used to characterize turbulent buoyant convection in a box-shaped Rayleigh-Bénard cavity with a rough bottom plate made of a series of square based blocks separated by valleys. The cavity is filled with water. The Rayleigh number varies over five decades up to 10^{10}. As mentioned in the literature, three successive heat transfer regimes are identified: from inactive roughness (I) to a regime (III) where the heat transfer increase is larger than the one expected from the only surface increase due to roughness. The heat transfers of the transitional regime II are particularly intense. After validation against experimental and numerical data from literature, we highlight the role of the fluid retained within valleys (the inner fluid). It is shown that the heat transfer through the fluid interface between the cavity bulk and the inner fluid is strongly related to the overall heat transfer at the rough plate, with an exponent of the heat transfer scaling law close to 1/2 in the regime II. We found that this regime is active when the height of the roughness is larger than the thermal boundary layer thickness but, still, enfolded within the kinetic boundary layer. As compared to regimes I and III, regime II is characterized by larger temperature fluctuations, especially near the rough plate, and a larger friction coefficient. A fluctuating rough fluid layer overlaying both blocks and valleys appears in the regime III, in addition to the classic boundary layers formed along the plate geometry.

Key words: Bénard convection, turbulent convection, roughness

---

† Email address for correspondence: anne.sergent@sorbonne-universite.fr

1. Introduction

The addition of wall roughness in thermal systems involving turbulent convection is a common strategy to enhance the heat transfer of industrial systems. Roughness also constitute a major factor in many turbulent flows met in nature. To explain the physical mechanisms involved in a flow interacting with roughness and at the origin of the intensification of heat transfer, many efforts have been made in the specific case of Rayleigh-Bénard (RB) convection (Chillà & Schumacher 2012). The classic RB convection consists in a fluid flow enclosed in a cavity heated from the bottom and cooled at the top. The corresponding flow depends on the following main control parameters: the Rayleigh number, Ra, the Prandtl number, Pr, and the cavity aspect ratio, Γ, while the main response of the system can be expressed in terms of a dimensionless heat transfer i.e. by means of the Nusselt number, Nu. The dependence of the Nusselt number on the control parameters ($Nu \sim \alpha Ra^{\beta} Pr^{\zeta}$) has been widely investigated (Ahlers *et al.* 2009; Chillà & Schumacher 2012), and the unifying theory of Grossmann & Lohse (2000, 2001)(Stevens *et al.* 2013) has been proposed to describe the multiple scaling laws of Nu_{GL} in the $(Ra - Pr)$ parameter space.

In the case of turbulent RB convection with rough plates, three successive heat transfer regimes have been observed as Ra is increased. It was first demonstrated experimentally by using a series of convection cavities with varying roughness aspect ratios λ, defined as the pyramid-shaped roughness height over its base (Xie & Xia 2017). It has been shown that the two transitions delimiting the enhanced heat transfer "regime II" occur when the thicknesses of thermal, then kinematic, boundary layers are of the same size as the roughness height H_p. Similar results were obtained by (Rusaouën *et al.* 2018) in a cylindrical water RB cavity, but horizontal plates were smooth at the top and roughened by rectangular shaped obstacles at the bottom. They found an increase of the scaling exponent β close to 0.5 in the regime II. A heat transfer scaling law similar to those of the smooth plate was further obtained in the regime III but with an increased prefactor. Several experimental studies describe results inside the regime II (Roche *et al.* 2001; Qiu *et al.* 2005; Tisserand *et al.* 2011; Wei *et al.* 2014), while other configurations correspond to the regime III (Du & Tong 1998; Wei *et al.* 2014). In both cases, the intensification of the emission of the thermal plumes from roughness is considered to be at the origin of the heat transfer increase. By means of a quantitative analysis of the plumes (Belkadi *et al.* 2020), it has been shown that the plume density and their velocity distribution are significantly affected by the presence of roughness, as compared to the case of a smooth plate. By introducing a critical Rayleigh number Ra_c defined as the Rayleigh number for which the thermal boundary layer has the size of the roughness height, (Rusaouën *et al.* 2018) succeeds to make collapsing results obtained in different asymmetric rough RB cavities over the three regimes, whatever the roughness shape.

Given its efficiency to transfer heat, many recent works have attempted to optimize the regime II and to extend its Ra-range of existence by modifying roughness geometry (Toppaladoddi *et al.* 2015, 2017; Xie & Xia 2017; Jiang *et al.* 2018; Xia 2019; Zhu *et al.*

2019). These studies have adopted sinusoidal-shaped roughness blocks in two-dimensional direct numerical simulations (DNS) or pyramid-shaped roughness blocks in experiments. They introduced an additional geometric parameter λ describing the roughness in terms of wavelength or pyramid aspect ratio (λ is the height over the base of the element). In all these cases, it has been demonstrated that the roughness density as well as λ increase the β scaling exponent to a value close to $1/2$, at least inside a particular range of Ra. Similar trends have been obtained in the case of rectangular blocks. Wagner & Shishkina (2015) and Emran & Shishkina (2020) performed three-dimensional DNS in cubic or cylindrical domains where the roughness is modelled respectively by large size straight or cylindrical bars. The influence of the gap width (g) between blocks and of the roughness height (H_p) on the heat transfer and on the flow structure has been documented for Rayleigh numbers up to $5 \cdot 10^8$ and $Pr \sim 1$. Bulk flow has been shown to be enhanced both by increasing H_p and g, while the secondary flow circulations located inside the obstacle gap weakens as the width of the obstacle increases. This leads to an increase of Nu whereas H_p and g become larger than the thermal boundary layer thickness. The influence of rectangular-shaped obstacles on the flow has been previously investigated experimentally at higher Ra in a water-filled cavity (Salort *et al.* 2014; Liot *et al.* 2017). It has been shown that roughness does not clearly affect the mean flow, but enhances drastically velocity fluctuations in the whole cavity which results in a short logarithmic layer above the roughness blocks. Two potential mechanisms are put forward: a transition to a turbulent boundary layer above the roughened plate and a plume emission increase, which relative influences may vary with the roughness shape.

These previous studies demonstrate that the roughness geometry is a crucial factor in the alteration of flow and heat transfer, illustrating the key role of flow surrounding roughness blocks. Taking advantage of the full 3D information obtained from DNS, this paper aims at describing the evolution of fluid dynamics around the roughness blocks for the three heat transfer regimes and to explain how it contributes to enhance heat transfer.

To this purpose, we simulate the flow inside an asymmetric RB cavity with a bottom plate roughened by box-shaped obstacles. This asymmetric geometry allows to study separately the smooth and rough plates in a single simulation, provided that the bulk temperature is considered (Tisserand *et al.* 2011; Salort *et al.* 2014). Still, due to resolution requirements, numerical studies are usually performed with simplified geometries (macroscopic scale roughness blocks, in limited numbers, with specific symmetries or quasi-two-dimensional geometry), or at moderate Rayleigh numbers (Wagner & Shishkina 2015; Zhu *et al.* 2019; Emran & Shishkina 2020). To overcome this difficulty, we set H_p at a particular value which locates the first transition between regimes I and II at a moderate Ra (here around 10^7). Both transition regimes are then feasible at intermediate Rayleigh numbers (less than 10^{10}) with a reasonable mesh size. This range of Rayleigh numbers corresponds to the experimental study of Tummers & Steunebrink (2019). Worth to be noted that it is also two to three decades smaller than in the previous experiments using

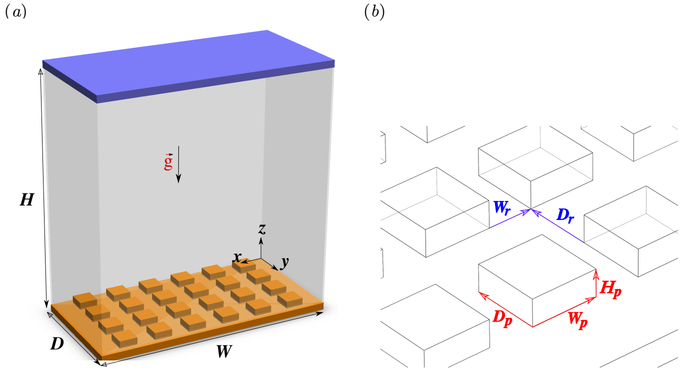

FIGURE 1. (*a*) Asymmetric Rayleigh-Bénard cavity (***R/S***) with a rough bottom plate. (*b*) Characteristic lengths of the block spatial arrangement.

water (Wei *et al.* 2014; Xie & Xia 2017; Rusaouën *et al.* 2018). Furthermore, the resulting H_p leads to a spatial arrangement of box-shaped blocks in sufficient numbers to consider that the influence of the flow along the vertical walls is negligible in the cavity central part.

In this paper, we report DNS results covering five decades in Rayleigh number. The main objective is to determine whether the two successive heat transfer regime transitions can be captured numerically in a single physical set-up. Then, we investigate which physical mechanisms in the neighbourhood of the roughness blocks may explain the enhanced heat transfer of the regimes II and III. In particular, we seek to identify the respective roles of the flow above the top surface of the blocks, and of the fluid circulating within the roughness valleys (called the inner fluid). Finally, we examine how the flow dynamics is altered by the regime changes.

The paper is organized as follows. Section 2 introduces the physical and numerical problem. Section 3 presents the roughness effect on the global heat transfer for the three heat transfer regimes and compares the DNS results to experimental data. Next, the study details the respective contributions of the roughness blocks and the inner fluid retained between them, to global heat transfer in section 4. Finally, the roughness effect on the fluid flow is described in section 5.

2. Physical configuration and governing equations

2.1. *Physical setup*

We study the fluid flow occurring in an asymmetric RB rectangular cavity with a rough bottom plate as sketched in figure 1. The geometrical aspect ratios are set at $\Gamma_x = W/H = 1$ and $\Gamma_y = D/H = 0.5$ where H is the height, D the depth and W the width of the cavity. The smooth cold top plate (resp. the hot bottom plate including roughness blocks) is isothermal at the constant temperature T_S (resp. T_R). Vertical side-walls are considered to be adiabatic. No-slip conditions are imposed on walls. The physical problem depends on the Rayleigh number defined as $Ra = \alpha g \Delta T H^3/\nu\kappa$ and the Prandtl number ($\mathrm{Pr} = \nu/\kappa$), where α is the volumetric thermal expansion coefficient, g the gravity, $\mathit{\Delta} T = T_R - T_S$ the temperature difference, ν the kinematic viscosity and κ the thermal diffusivity. The Prandtl number is taken equal to 4.38, that corresponds to taking water as the working fluid at the mean temperature of $40°C$.

The roughness is modelled by a set of square-based blocks. We call *valley* the fluid space present between the blocks. The typical size of the blocks (width W_p, depth D_p and height H_p) and their horizontal distribution (D_r,W_r) have been chosen to meet two criteria: (i) A roughness height sufficiently large to obtain the first transition between regimes I and II at a Rayleigh number close to 10^7 ; (ii) A spatial distribution of roughness blocks sufficiently close to Lyon's experiments (Salort *et al.* 2014) to facilitate comparison.

Accordingly, we set the roughness height to $H_p = 0.03H$. Following Rusaouën *et al.* (2018), we estimate the critical Rayleigh number (Ra_c) of the first transition equal to $Ra_c = 9 \cdot 10^6$ based on an approximation of the thickness of the thermal boundary layer (δ_θ) estimated from the Grossman-Lohse (GL) theory (Stevens *et al.* 2013). The retained shape and distribution of roughness blocks ($W_p = 0.075H$, $D_p = 0.075H$, $H_p = 0.03H$ and $W_r = 0.075H$, $D_r = 0.05H$, see figure 1 for definitions) is equivalent to Lyon's experiment (Salort *et al.* 2014), leading to attach four rows of six box-shaped blocks to the bottom plate. The resulting ratio between the heat-exchange surface (A) of the asymmetric cavity and that of a fully symmetrical smooth cavity (hereafter respectively denoted as R/S and S/S) is equal to $C_s = (A_R + A_S)/(2A_S) = 1.216$, where A_S (A_R) stands for the dimensionless area of the smooth and the rough plates respectively.

2.2. *Governing equations and system response*

We solve the Navier-Stokes equations under the Boussinesq approximation. Dimensionless equations are written in the following form considering H, $\mathit{\Delta} T$ and $\dfrac{\kappa}{H}\sqrt{Ra}$ as reference scales for the length, the temperature and the velocity

$$\boldsymbol{\nabla} \cdot \boldsymbol{u} = 0 \tag{2.1a}$$

$$\partial_t \boldsymbol{u} + \boldsymbol{u} \cdot \boldsymbol{\nabla} \boldsymbol{u} = -\boldsymbol{\nabla} P^* + \mathrm{Pr}\, Ra^{-\frac{1}{2}} \boldsymbol{\nabla}^2 \boldsymbol{u} + \mathrm{Pr}\, \theta \boldsymbol{e_z} \tag{2.1b}$$

$$\partial_t \theta + \boldsymbol{u} \cdot \boldsymbol{\nabla} \theta = Ra^{-\frac{1}{2}} \boldsymbol{\nabla}^2 \theta \tag{2.1c}$$

where $\boldsymbol{u} = (u, v, w)$ is the velocity vector, t the time, P^* the dimensionless driving pressure, θ the temperature, and $\boldsymbol{e_z}$ the unit vector in the vertical upward direction. The temperature of top cold plate is taken as reference, so that the dimensionless temperature θ ranges from $\theta_S = 0$ to $\theta_R = 1$.

The response of the system to the temperature difference $\mathit{\Delta} T$ applied on the two horizontal plates is measured in terms of dimensionless heat transfer by the local Nusselt number

$$Nu(\boldsymbol{x}, t) = \sqrt{Ra} \times w(\boldsymbol{x}, t) \times \theta(\boldsymbol{x}, t) - \partial_z \theta(\boldsymbol{x}, t), \tag{2.2}$$

where $\boldsymbol{x} = (x, y, z)$ is the coordinate vector. We note $Nu_{R/S}$, the time and space average of $Nu(\boldsymbol{x},t)$ over the fluid volume contained in the upper part of the asymmetrical RB cavity for $z \geqslant H_p$. Similarly, $Ra_{R/S}$ refers hereafter to the Rayleigh number imposed to the asymmetric cavity.

Due to the geometrical asymmetry of the configuration, the bulk temperature θ_{bulk} is no longer equal to the mean between smooth and rough plates temperatures, i.e. $\theta_{bulk} \neq (\theta_R+\theta_S)/2$. The temperature difference between the bulk region and the hot plate (respectively the cold plate) is called $\Delta\theta_R$ (resp. $\Delta\theta_S$). Following Tisserand *et al.* (2011), we assume that the top and bottom parts of the cavity are independent. Consequently, one can define two additional Rayleigh and Nusselt numbers related to each plate as follows,

$$\left\{\begin{array}{llcll} \Delta\theta_S & = 2 \times (\theta_{bulk} - \theta_S) & , & \Delta\theta_R & = 2 \times (\theta_R - \theta_{bulk}) \\ Ra_S & = Ra_{R/S} \times \Delta\theta_S & , & Ra_R & = Ra_{R/S} \times \Delta\theta_R \\ Nu_S & = Nu_{R/S} \, / \, \Delta\theta_S & , & Nu_R & = Nu_{R/S} \, / \, \Delta\theta_R \end{array}\right. \tag{2.3}$$

where we denote by Ra_S (respectively Ra_R) and Nu_S (resp. Nu_R) the Rayleigh and Nusselt numbers related to the smooth (resp. rough) plate. This is equivalent to taking into account different reference heat fluxes ($\Phi_R^{ref} = A_S\Delta\theta_R$ and $\Phi_S^{ref} = A_S\Delta\theta_S$, here expressed dimensionless).

2.3. *Numerical methods and validation*

A finite volume approach is applied to discretize the governing equations (eq. 2.1), by means of the in-house SUNFLUIDH solver. A centred scheme is used for the spatial discretization on a staggered grid and the time discretization is done by second order backward differentiation scheme. The diffusive terms are implicitly treated while convective terms are estimated by the Adams-Bashforth method. This leads to a Helmholtz-like equation for each velocity component and the temperature, which is solved by applying the Alternating Direction Implicit method. The incompressibilty constraint is ensured by using a prediction-projection method (Goda 1979; Guermond *et al.* 2006). The resulting Poisson's equation for the pressure is solved by a multi-grid method coupled to the iterative Successive Over-Relaxed algorithm (Strang 2007). A domain decomposition method is implemented using MPI as well as OpenMP in order to increase the level of parallelism. In this context, the Alternating Direction Implicit method is completed by a Schur decomposition technique. Roughness blocks are not modelled, because we have defined body-fitted meshes. As a consequence, standard boundary conditions are applied to all wall boundary conditions.

SUNFLUIDH code is a general purpose solver for modelling quasi-incompressible fluid flows, like rotating flows with free interface (Yang *et al.* 2020), turbulent flows (Derebail Muralidhar *et al.* 2019) or multi-physics studies (Hireche *et al.* 2020).

Computations are performed for a large range of Rayleigh numbers ($Ra \in [10^5 : 10^{10}]$) in order to cover the three heat transfer regimes. Details about the test cases can be found in table 1. An irregular mesh is constructed for each test case in order to resolve

$Ra_{R/S}$	$N_x \times N_y \times N_z$	τ	$Nu_{R/S}$	Ra_S	Nu_S	Ra_R	Nu_R
10^5	$320 \times 200 \times 320$	$/^{(1)}$	3.8	$9.96 \cdot 10^4$	3.8	$1.00 \cdot 10^5$	3.8
$2 \cdot 10^5$	$320 \times 200 \times 320$	$/^{(1)}$	4.8	$2.00 \cdot 10^5$	4.8	$2.00 \cdot 10^5$	4.8
$5 \cdot 10^5$	$320 \times 200 \times 320$	300	6.3	$5.03 \cdot 10^5$	6.3	$4.97 \cdot 10^5$	6.4
10^6	$320 \times 200 \times 320$	400	8.0	$1.01 \cdot 10^6$	7.9	$9.90 \cdot 10^5$	8.0
$2 \cdot 10^6$	$320 \times 200 \times 320$	500	10.0	$2.04 \cdot 10^6$	9.9	$1.96 \cdot 10^6$	10.2
$5 \cdot 10^6$	$320 \times 200 \times 320$	460	13.5	$5.23 \cdot 10^6$	12.9	$4.77 \cdot 10^6$	14.2
10^7	$320 \times 200 \times 320$	300	17.9	$1.06 \cdot 10^7$	16.8	$9.36 \cdot 10^6$	19.1
$2 \cdot 10^7$	$320 \times 200 \times 320$	300	23.1	$2.19 \cdot 10^7$	21.0	$1.81 \cdot 10^7$	25.5
$5 \cdot 10^7$	$512 \times 256 \times 512$	450	31.9	$5.68 \cdot 10^7$	28.1	$4.32 \cdot 10^7$	36.9
10^8	$512 \times 256 \times 512$	430	40.6	$1.16 \cdot 10^8$	35.1	$8.42 \cdot 10^7$	48.2
$2 \cdot 10^8$	$512 \times 256 \times 512$	450	51.0	$2.36 \cdot 10^8$	43.2	$1.64 \cdot 10^8$	62.1
$5 \cdot 10^8$	$768 \times 384 \times 768$	287	68.4	$5.97 \cdot 10^8$	57.3	$4.03 \cdot 10^8$	84.9
10^9	$768 \times 384 \times 768$	220	85.9	$1.20 \cdot 10^9$	71.7	$8.02 \cdot 10^8$	107.1
$2 \cdot 10^9$	$768 \times 384 \times 768$	200	107.0	$2.40 \cdot 10^9$	89.2	$1.60 \cdot 10^9$	133.7
$5 \cdot 10^9$	$768 \times 384 \times 768$	200	144.6	$5.98 \cdot 10^9$	120.9	$4.02 \cdot 10^9$	179.8
10^{10}	$1024 \times 512 \times 1024$	155	179.5	$1.20 \cdot 10^{10}$	149.6	$8.00 \cdot 10^9$	224.4

TABLE 1. Computational parameters and dimensionless heat transfers: $Ra_{R/S}$, Rayleigh number imposed to the cavity; $N_x \times N_y \times N_z$, mesh size; τ, time period used for statistics in dimensionless time units; $Nu_{R/S}$, the Nusselt number in the R/S cavity; (Ra_S, Nu_S), the Rayleigh and Nusselt numbers corresponding to the smooth part of the cavity; (Ra_R, Nu_R), idem for the rough part of the cavity (see eq. 2.3). $^{(1)}$ Note that for $Ra \leqslant 2 \times 10^5$ the flow is stationary.

the Kolmogorov microscale (η). The mesh size never exceeds 0.55η (or 0.76η) between blocks (or within the cavity bulk respectively).

The space and time convergence of statistics have been verified by computing the global Nusselt number from different formulations as proposed by Stevens *et al.* (2010). This methodology remains applicable for $z \geqslant H_p$ due to the adiabatic sidewalls. The obtained values converge with a deviation smaller than 1% around the mean value ($Nu_{R/S}$).

The code SUNFLUIDH has been validated in classic RB configuration beforehand. For this purpose, simulations have been performed in a fully smooth cavity (called S/S) of aspect ratio $\mathit{\Gamma}_y = 0.5$ filled with water for Rayleigh numbers up to $Ra = 2 \cdot 10^9$, in order to compare with Kaczorowski *et al.* (2014) data. A very good agreement is obtained for the compensated Nusselt number ($NuRa^{-1/3}$), as shown in figure 2.

3. Roughness effect on the global heat transfer

3.1. *Global heat transfer measured in the asymmetric cavity*

The influence of roughness on the heat transfer is first brought to light by comparing the responses of a fully smooth cavity (S/S) and of the asymmetric cavity (R/S). The effect of the roughness on heat transfer due to the increase of the heat exchange surface area ($C_s \times Nu_{S/S}$) is plotted as an indication. Three regimes of heat transfer clearly appear for the R/S cavity in the figure 2. (i) A reduction of the Nusselt number $Nu_{R/S}$

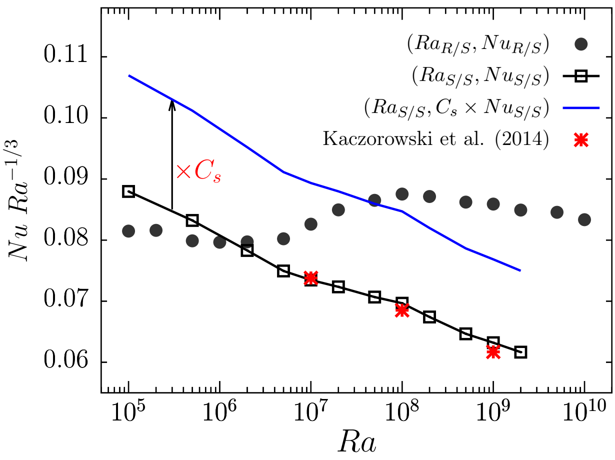

FIGURE 2. Compensated Nusselt number as a function of Rayleigh number for the fully smooth cavity (S/S) and the asymmetric cavity (R/S). The blue line corresponds to the Nusselt number increased by the factor C_s (corresponding to the relative increase of the heat exchange surface in the (R/S) cavity). Red points refer to DNS results from Kaczorowski *et al.* (2014).

comparing with $Nu_{S/S}$ is observed at low Rayleigh numbers for one decade in the range $Ra \lesssim 10^6$. This phenomenon has already been described experimentally (Tisserand *et al.* 2011) or using two-dimensional simulations (Zhang *et al.* 2018). (ii) For $Ra \gtrsim 10^8$, an increase of the Nusselt number $Nu_{R/S}$ compared to the S/S cavity is obtained, that exceeds the relative increase due to additional surface induced by roughness blocks as reported in previous works (Tisserand *et al.* 2011). (iii) In-between, a transitional regime is present, corresponding to an enhancement of the heat transfer.

The following section aims to verify whether the effect of roughness on the heat transfer of each of the two plates, whether smooth or rough, is the same as that observed in the asymmetrical cavity.

3.2. *Analysis of the scaling laws based on the approach of plates separation*

We use the plate separation method to identify respective behaviours of the smooth and rough plates, as proposed by Tisserand *et al.* (2011). The resulting (Ra_S, Nu_S) and (Ra_R, Nu_R) (see equations 2.3 and table 1) are plotted in figure 3. First, we note that the heat transfer on the smooth plate (Nu_S) follows a single $Nu-Ra$ scaling law. Conversely, the heat transfer on the rough plate (Nu_R) clearly presents two changes in the scaling law, around $Ra_R \sim 3 \cdot 10^6$ and $1.2 \cdot 10^8$. We note that the critical Rayleigh number ($Ra_c = 9 \cdot 10^6$) is in between, which is explainable by the increase of the heat transfer in the presence of roughness.

As a result, three heat transfer regimes can be identified on the rough plate, in agreement with previous experimental studies (Xie & Xia 2017; Rusaouën *et al.* 2018; Tummers & Steunebrink 2019). In the regime I, no difference between the rough and the smooth plate are distinguishable. In the regime III, the rough plate presents a scaling law exponent β almost similar to the regime I and close to the classic value 1/3. But

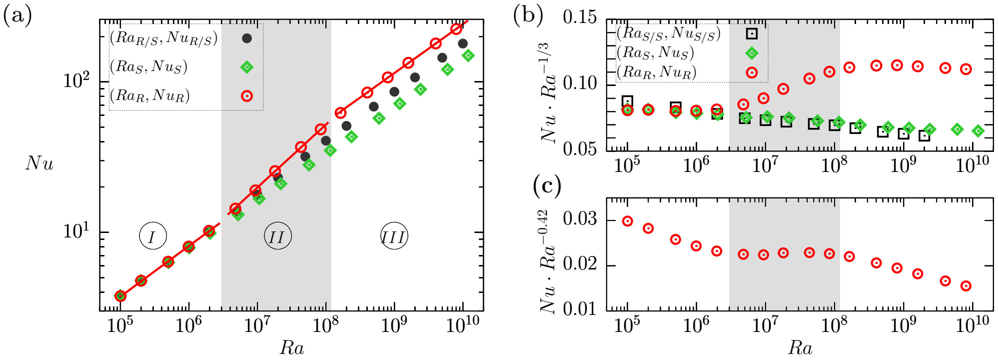

FIGURE 3. (a) Comparison of the Rayleigh-scaling of the Nusselt numbers for the asymmetric R/S cavity, the smooth S/S cavity or for the rough R and the smooth S plates. (b,c) Compensated Nusselt numbers. The solid lines correspond to the least-squares fits of the R plate results for the three regimes: regime I: $Nu_R \sim 0.078 Ra_R^{0.34}$, regime II: $Nu_R \sim 0.024 Ra_R^{0.42}$ and regime III: $Nu_R \sim 0.136 Ra_R^{0.33}$. The shaded area marks the $Ra-$range of the regime II.

the prefactor α is smaller for regime I than for regime III. In contrast, the regime II corresponds to an exponent of $\beta \sim 0.42$, indicating an intensified heat transfer. Figure 3-c is used as a basis for setting the limits for regime II. The range of Ra numbers thereby determined, will be shaded on all the figures in the rest of the article.

To summarize, roughness enhances the heat transfer either by increasing the exponent β (regime II) or the prefactor α of the $(Nu - Ra)$ scaling law in the regime III for simulations up to $Ra = 10^{10}$. This suggests that the regime II can be seen as a transitional regime, after which the flow would revert to a classic organization. However, it is worthy noted that in Regime III, the overall heat transfer $Nu_{R/S}$ is larger than the simple additional contribution due to the increase in exchange surface area.

Results obtained in the S/S cavity have been added to the figure 3-b for comparison with the smooth plate (S). Generally speaking, a similar behaviour is observed for $Nu_{S/S}$ and Nu_S. This result is consistent with previous experimental observations (Tisserand *et al.* 2011; Wei *et al.* 2014). But we note in regime I that the heat transfer is slighly reduced by the addition of roughness in the asymmetric cavity when compared to the S/S cavity, as previously shown by (Tisserand *et al.* 2011; Zhang *et al.* 2018). An opposite effect is observed in the regime III, where Nu_S is slightly larger than $Nu_{S/S}$. A potential interpretation is that not only the thermal boundary layers are altered by the roughness, but also the dynamics of the bulk flow, as suggested by Wei *et al.* (2014).

3.3. *Comparison with experimental data*

Recently, Rusaouën *et al.* (2018) proposed to make use of the critical Rayleigh number (Ra_c) to bring out the effect of roughness on the heat transfer. It is based on the idea that the transition to the enhanced heat transfer regime (II) occurs when the thermal boundary layer thickness δ_θ becomes of the same size as roughness blocks. The authors obtained collapsed data, showing the same trend from the reduced heat transfer regime

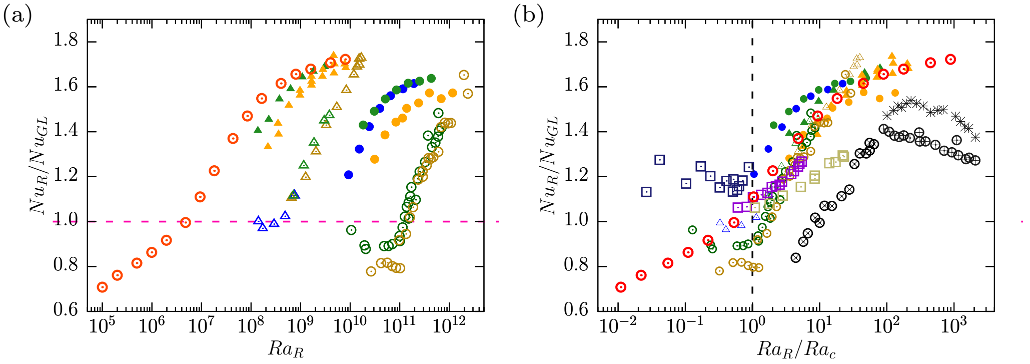

FIGURE 4. Comparison of the normalized heat transfer on the rough plate with experimental data. Nu_R is normalized by the Grossmann - Lohse model (Nu_{GL}) estimated from (Stevens *et al.* 2013). DNS data are plotted with red open circles (○). Symbols correspond to experimental data: $H_p = 2mm$ in the small cavity (△△△), or the tall R/S cylindrical cavity (○○) from Tisserand *et al.* (2011); $H_p = 4mm$ in the small cavity (▲▲) or the tall R/S cylindrical cavity (●●●) from Rusaouën *et al.* (2018); $H_p = 3mm$ R/S (⊗), $H_p = 8mm$ S/R (⊕) and $H_p = 8mm$ R/S ($*$) in a cylindrical cavity with pyramid-shaped roughness blocks from Wei *et al.* (2014) ; $H_p = 2mm$ in a R/S rectangular cavity (□□□) from Salort *et al.* (2014).

(I) for $Ra_R < Ra_c$ to an increased regime (III), when applied to experiments performed in asymmetric RB cavities.

Despite a gap of three $Ra-$decades between our physical configuration and the displayed experiments, the present DNS results agree well with this physical representation (figure 4). The figure 4-b retains the reduced variables ($Nu_R/Nu_{GL}; Ra_R/Ra_c$) to compare our DNS data with experiments performed in water. The shape of the experimental containers are either cylindrical (Tisserand *et al.* 2011; Wei *et al.* 2014; Rusaouën *et al.* 2018) or rectangular (Salort *et al.* 2014). The roughness is made by square-based blocks, except the Wei *et al.* (2014) set-up, where pyramid-shape blocks are used.

Normalization by the respective Ra_c for each data set allows to bring together most results including our numerical data, which fit a similar trend of Nu increase, especially with Lyon's data. In particular, the agreement is remarkable during the regime II. This result was expected, as we use comparable shape and distribution of roughness blocks. In contrast, a clear decreasing Nu for $Ra_R/Ra_c \geqslant 10^2$ is reported by Wei *et al.* (2014), when using pyramid-shape roughness. This illustrates the potential influence of the 3D flow dynamics around roughness blocks on the global heat transfer.

4. Contribution of the inner fluid to the heat transfer

The heat transfer regime depends strongly on the pair (Rayleigh number ; height of roughness blocks), as shown by the unifying aspect of Ra_c. In the R/S cavity, the vertical heat flux (Nu) below the roughness height is smaller than its global value ($Nu\ (z < H_p) < Nu_{R/S}$) due to the horizontal contribution originated from the vertical surfaces of the roughness blocks. Conversely, $Nu(z \geqslant H_p) = Nu_{R/S}$, because of the adiabaticity of the

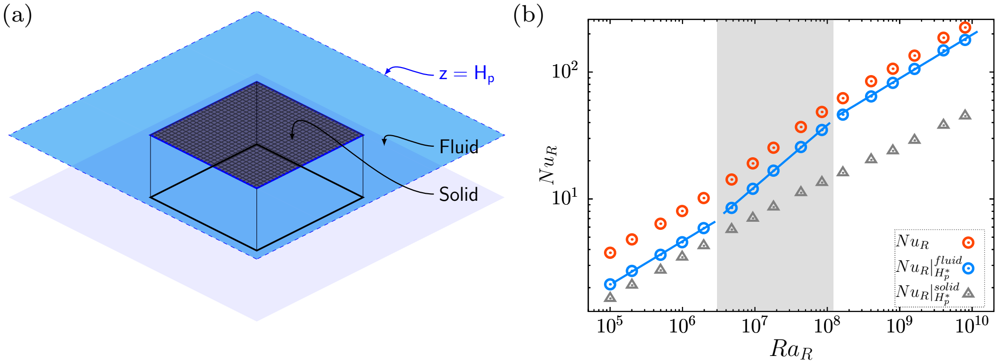

FIGURE 5. (a) Sketch of the geometric division of the horizontal plane at $z = H_p$. (b) Separation of rough heat flux at $z = H_p$ (noted $Nu_R|_{H_p}$) into contribution from the fluid interface ($Nu_R|^{fluid}_{H_p}$) and from the solid surface ($Nu_R|^{solid}_{H_p}$). The solid lines correspond to the least-squares fits of the results on the fluid interface for the three regimes: regime I: $Nu_R|^{fluid}_{H_p} \sim 0.041 Ra_R^{0.34}$; regime II: $Nu_R|^{fluid}_{H_p} \sim 0.005 Ra_R^{0.49}$; regime III: $Nu_R|^{fluid}_{H_p} \sim 0.072 Ra_R^{0.34}$. The shaded area marks the $Ra-$range of the regime II.

vertical sides of the cavity. This is also valid for Nu_R, the heat flux in the rough part of the cavity. Consequently, Nu_R results from both the dynamics of the thermal boundary layer above the roughness blocks and the dynamics of the inner fluid retained within roughness valleys. The heat flux measured at $z = H_p$ is an indicator of both dynamics.

In order to gain insights into the mechanisms of heat exchange at the roughness height, we first focus on the rough heat flux Nu_R at $z = H_p$, noted hereafter $Nu_R|_{H_p}$. $Nu_R|_{H_p}$ is contributed from two complementary surfaces (see figure 5-a): (i) the top surface of the *solid* blocks, referred to as $Nu_R|^{solid}_{H_p}$, and (ii) the *fluid* interface between the bulk of the cavity and the inner fluid retained within roughness valleys, referred to as $Nu_R|^{fluid}_{H_p}$. The heat transfer across the fluid interface at $z = H_p$ ($Nu_R|^{fluid}_{H_p}$) can be divided into two contributions, depending on the heat transfer mode, a conductive ($Nu_R^{cd}|^{fluid}_{H_p}$) and convective ($Nu_R^{cv}|^{fluid}_{H_p}$) parts. It leads to the following expression

$$Nu_R|_{H_p} = Nu_R|^{solid}_{H_p} + Nu_R^{cd}|^{fluid}_{H_p} + Nu_R^{cv}|^{fluid}_{H_p} \tag{4.1}$$

with

$$Nu_R|^{solid}_{H_p} = \frac{1}{\Delta\theta_R\, A_S} \int_{A_{solid}} -\partial_z \langle\overline{\theta}\rangle_{A_{solid}} ds; \tag{4.2}$$

$$Nu_R^{cd}|^{fluid}_{H_p} = \frac{1}{\Delta\theta_R\, A_S} \int_{A_{fluid}} -\partial_z \langle\overline{\theta}\rangle_{A_{fluid}} ds; \tag{4.3}$$

$$Nu_R^{cv}|^{fluid}_{H_p} = \frac{1}{\Delta\theta_R\, A_S} \int_{A_{fluid}} \sqrt{Ra_{R/S}}\ \langle\overline{w\theta}\rangle_{A_{fluid}} ds, \tag{4.4}$$

where A_{solid} (A_{fluid}) is the total area of the top surface of all blocks (of the fluid interface at $z = H_p$ respectively), i.e. $A_S = A_{solid} + A_{fluid}$. The notations $\langle\phi\rangle_A$ and $\overline{\phi}$ stand for the space average over the horizontal surface area A and the time average of the variable ϕ, respectively.

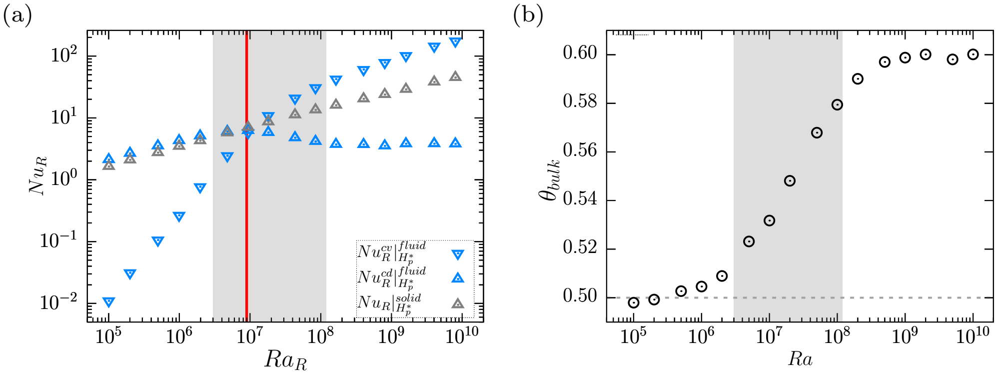

FIGURE 6. (a) Comparison of the different contributions from the solid surface ($Nu_R^{cd}|_{H_p}^{solid}$) and the fluid interface ($Nu_R^{cd}|_{H_p}^{fluid}$ and $Nu_R^{cv}|_{H_p}^{fluid}$) to the rough heat flux Nu_R at $z = H_p$ as a function of the rough Rayleigh number (Ra_R). The vertical red line marks the critical Rayleigh number (Ra_c). (b) Bulk temperature (θ_{bulk}) as a function of Ra. The shaded area marks the $Ra-$range of the regime II.

4.1. *Contributions from solid and fluid zones to the rough heat flux*

The figure 5-b compares the evolution of the global rough Nusselt number Nu_R as a function of Ra, with Nusselt numbers originated from the top solid surface of the blocks and from the fluid interface. First, it is shown that the three regimes of heat transfer observed on the ($Ra_R - Nu_R$) scaling law come mainly from a change of $Nu_R|_{H_p}^{fluid}$. The three power-law fittings for $Nu_R|_{H_p}^{fluid}$ are given in the caption of the figure 5. In agreement with previous 2D DNS or experiments with pyramid-shaped roughness (see for example Roche *et al.* (2001); Qiu *et al.* (2005); Toppaladoddi *et al.* (2017); Zhu *et al.* (2017)), we obtain a scaling exponent for the regime II close to 1/2 ($\beta = 0.49$). In contrast, $Nu_R|_{H_p}^{solid}$ is hardly modified by the successive regimes. It can be roughly associated with a single scaling exponent close to $\beta \approx 2/7$ as expected in the hard turbulence regime, that supposes diffusive thermal boundary layers (Castaing *et al.* 1989).

As a consequence, the physical mechanisms responsible of the two transitions between the successive heat transfer regimes appears being mainly driven by the fluid dynamics occurring within the valleys. This finding is consistent with manipulating the scaling laws of heat transfer through roughness wavelength modification (Toppaladoddi *et al.* 2015; Xie & Xia 2017; Zhu *et al.* 2019).

4.2. *Contributions of conduction and convection to the rough heat flux*

The heat transfer through the fluid interface depends both on the temperature field for its conductive part ($Nu_R^{cd}|_{H_p}^{fluid}$) and on the temperature and velocity fields for its convective part ($Nu_R^{cv}|_{H_p}^{fluid}$) (see equation 4.1). The figure 6-a illustrates this dividing. First, we observe that the three successive heat transfer regimes do not appear clearly with Ra increasing on this figure. But surprisingly, the critical Rayleigh number (Ra_c) seems to be becoming a significant parameter: when $Ra < Ra_c$, the conduction mode is dominant and the convection mode through the fluid interface negligible, while this is the opposite when $Ra > Ra_c$. A negligible convective heat transfer through the fluid interface does not mean that the fluid within valleys is at rest, but that the mass exchange between the valleys and the bulk is negligible. Around Ra_c, the three contributions to Nu_R are on the same order.

Besides, some specific features can be identified in the regimes I and III, the intermediate regime II appearing as transitional with athe competition between the conductive and convective modes at the fluid interface. In the regime I, $Nu_R|_{H_p}^{solid}$ and $Nu_R^{cd}|_{H_p}^{fluid}$ share a similar trend (in particular the exponent β of the scaling law in Ra), that is compatible with a diffusive boundary layer covering the top of blocks. In the regime III, the dominance of $Nu_R^{cv}|_{H_p}^{fluid}$ on Nu_R reveals an intensification of the mass exchange through the fluid interface. Concurrently, we observe a saturation of the conductive part of the heat transfer through the fluid interface, that forms a plateau around a constant value ($Nu_R^{cd}|_{H_p}^{fluid} \approx 3.7$). This is also the case for the bulk temperature that saturates around $\theta_{bulk} \sim 0.6$ in the regime III on the figure 6-b. This figure also demonstrates the up-down symmetry breaking of the temperature field in regimes II and III.

The dominance of convection and the saturation of θ_{bulk} and $Nu_R^{cd}|_{H_p}^{fluid}$ towards constant values suggest that the fluid is well mixed in the regime III, within the cavity bulk but also within the valleys. Considering uniform diffusive boundary layers of similar thickness covering the top and bottom walls, a simple thermal balance between the top and bottom walls gives an estimate of the bulk temperature as

$$\theta_{bulk}^* = \frac{A_R\,\theta_R + A_S\,\theta_S}{A_R + A_S}. \tag{4.5}$$

The asterisk (*) marks the theoretical estimate of variable. The above formula gives a good estimate of $\theta_{bulk}^* \simeq 0.59$, when compared to the asymptotic value of the figure 6-b. The bulk temperature in the regime III is thus only determined by the roughness geometry.

We now explain that it is also the case for $Nu_R^{cd}|_{H_p}^{fluid}$. At $z = H_p$, we cannot consider that the temperature is equal to θ_{bulk} due to the inhomogeneity imposed by the alternating of blocks and fluid interfaces. A fluid layer at an intermediate temperature (θ_i^*) results from mixing processes occurring above the roughness height. We refer hereafter to this layer as the fluctuating rough fluid layer.

Additionally, the inner fluid retained inside the valleys can be seen to act as small, well-mixed RB cells with a bulk temperature equal to the mixing temperature of the fluctuating rough layer (θ_i^*). This enables to define a film temperature of the inner boundary layer of valleys, which goes along the bottom wall, as $\theta_f^* = \frac{1}{2}\,(\theta_i^* + \theta_R)$. As a consequence, the conductive heat flux through the fluid interface exchanges heat between the fluctuating rough fluid layer at θ_i^* and the inner boundary layer at θ_f^*, as

$$Nu_R^{*cd}|_{H_p}^{fluid} = \frac{A_{fluid}}{A_S \Delta\theta_R}\,\frac{\left(\theta_f^* - \theta_i^*\right)}{H_p} \qquad \text{with} \qquad \theta_i^* = \frac{A_{fluid}}{A_S}\theta_{bulk}^* + \frac{A_{solid}}{A_S}\theta_R\,. \tag{4.6}$$

This reasoning leads to a theoretical estimate of $Nu_R^{*cd}|_{H_p}^{fluid} \simeq 4.5$ for the regime III,

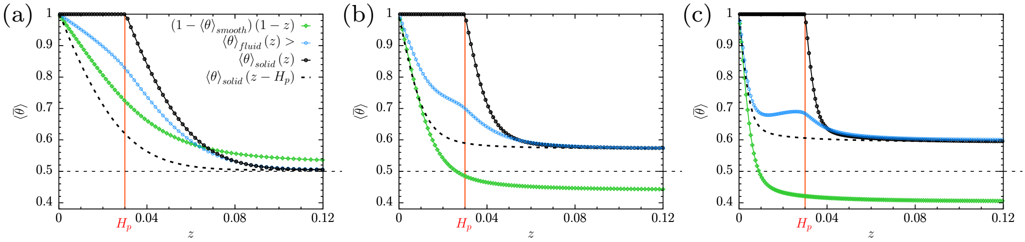

FIGURE 7. Space and time averaged vertical temperature profiles in the solid, fluid and smooth zones for three particular Ra: (a) $Ra = 2 \cdot 10^6$ (regime I) ; (b) $Ra = 5 \cdot 10^7$ (regime II) ; (c) $Ra = 10^9$ (regime III). The profile for the smooth zone (in green) has been reflected in $(1-z; 1-\theta)$ allowing the comparison with rough zone profiles. A profile offset by the distance H_p is plotted for the solid zone with a dashed black line. The red line marks the roughness height H_p.

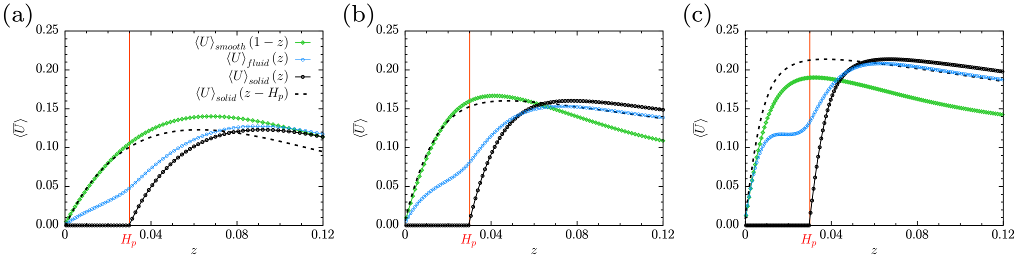

FIGURE 8. Space and time averaged vertical profiles of the horizontal velocity magnitude ($U = \sqrt{u^2+v^2}$) in solid, fluid and smooth zones for three particular Ra: (a) $Ra = 2 \cdot 10^6$ (regime I) ; (b) $Ra = 5 \cdot 10^7$ (regime II) ; (c) $Ra = 10^9$ (regime III). A profile offset by the distance H_p is plotted for the solid zone with a dashed black line. The red line marks the roughness height H_p.

which is in good agreement with the DNS result. It suggests that, in the regime III, the global thermal organization of the cavity is fixed by the geometry, with a diffusive and viscous boundary layers following the geometry of the roughness and a thicker fluctuating rough fluid layer overlaying roughness, the rest of the cavity being well mixed including the inner fluid.

5. Effect of roughness on the flow structure

5.1. *Boundary layers along the plate centre*

In this section, we focus on a restrictive volume of the cavity far from the vertical side-walls, in order to describe the mean boundary layers developing along the top solid surface of the blocks, or within the valleys and above. To do this, we retain the spatial division methodology of the previous section (in terms of solid or fluid zones), but only considering eight of the twenty-four blocks located in the centre of the bottom plate, or their direct fluid neighbourhood. Before focusing on the evolution of the boundary layer (BL) thicknesses with the heat transfer regimes, we present the space and time averaged vertical profiles of the temperature and horizontal velocity fields close to the top and

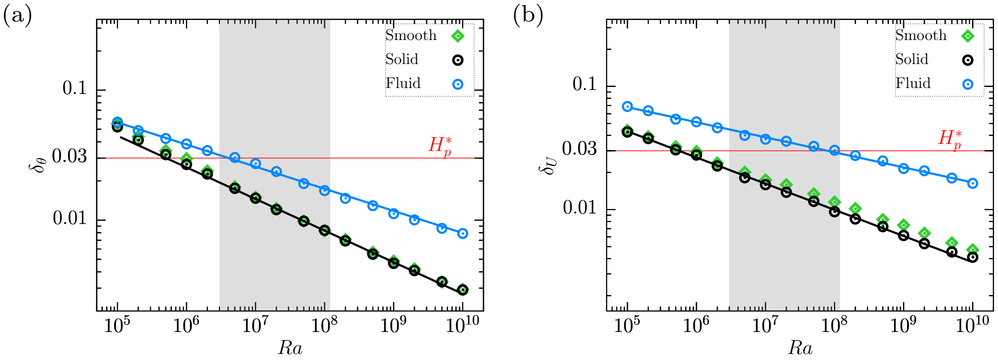

FIGURE 9. Displacement boundary layer thicknesses as a function of Ra and for each space-averaging zone (smooth, solid and fluid). (*a*) Thermal thickness δ_θ, (*b*) Kinetic thickness δ_U. The shaded area illustrates the $Ra-$range of the regime II. The red line marks the roughness height (H_p). The black and blue solid lines correspond to the least-squares fits of the results for the solid and fluid zones $\delta_\theta^{solid} \sim 0.90Ra^{-0.25}$, $\delta_\theta^{fluid} \sim 0.42Ra^{-0.17}$, $\delta_U^{solid} \sim 0.50Ra^{-0.21}$, $\delta_U^{fluid} \sim 0.28Ra^{-0.12}$.

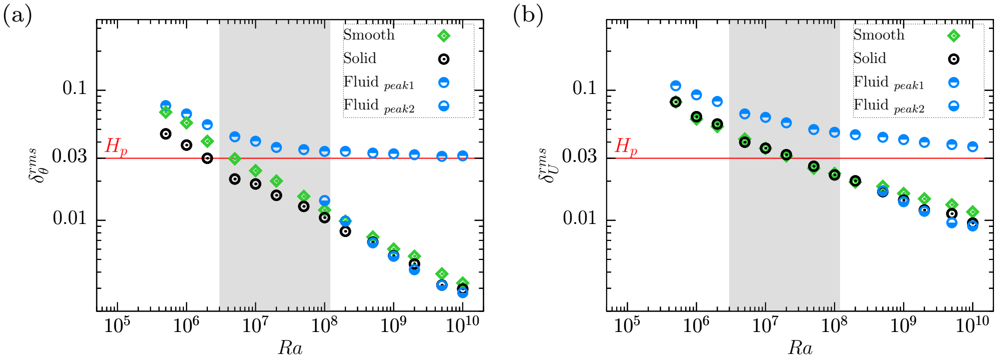

FIGURE 10. RMS-based boundary layer thicknesses as a function of Ra and for each space-averaging zone (smooth, solid and fluid). See equations 5.1 and 5.2 for definitions. (*a*) Thermal boundary layer thickness δ_θ^{rms} measured as the peak of θ_{rms}; (*b*) kinetic BL thickness measured as the peak of U_{rms}. The shaded area illustrates the $Ra-$range of the regime II. The red line marks the roughness height (H_p).

bottom plates. The horizontal velocity is defined as $U = \sqrt{u^2 + v^2}$. For clarity reason, we consider three particular Ra belonging to the three regimes, as shown in the figures 7 and 8.

As expected, we observe that the thermal BL located along the block top surface and the smooth plate becomes thinner with Ra. But surprisingly, in the regimes II and III, the temperature profiles above blocks and close to the smooth plate appears to be similar in near wall region, although the bulk temperature value is not equal to the mean temperature of plates ($(\theta_S + \theta_R)/2$). The temperature profile in the fluid zone is more complicated. In the regime I, a slow decrease of the temperature is observed in the valleys. In the regime II, the decrease is more pronounced, but with a change of slope as z passes through H_p. This slope change illustrates the onset of the convective heat transfers between the bulk of the cavity and the inner fluid of valleys. In the regime III, the temperature shows a quasi-plateau in the centre of valleys (see figure 7-c), confirming the presence of a kind of secondary well-mixed cells within valleys. Similar interpretations can be drawn for the viscous BL. In particular, within the valleys, the horizontal velocity increases with the heat transfer regime, up to presenting a plateau in the regime III that we can liken to a mean wind (figure 8-c).

As seen above, the temperature distribution and the fluid flow within valleys do not present a classic BL shape. As a consequence, we consider the displacement thickness definition, to take into account of inhomogeneity of the temperature and velocity fields, especially within the valleys. The definitions of the thermal and viscous BL thicknesses (δ_θ and δ_U) are as follows,

$$\delta_\theta = \int_0^{0.5} \left(\frac{\langle \overline{\theta} \rangle_A(z) - \theta_{bulk}}{\theta_R - \theta_{bulk}} \right) dz \tag{5.1}$$

$$\delta_U = \int_0^{z_0} \left(1 - \frac{\langle \overline{U} \rangle_A(z)}{U_0} \right) dz \qquad \text{with} \tag{5.2}$$

$$U_0 = max(\langle \overline{U} \rangle_A(z) : 0 \leqslant z \leqslant 0.5) \;\; \text{and} \;\; z_0 = z(\langle \overline{U} \rangle_A = U_0)$$

The BL thicknesses can be measured over the smooth plate, but also separately above the block top surfaces and the fluid interfaces, following the methodology proposed at the beginning of the present section. Their Ra-dependences are plotted in the figure 9. First, we note that a single law (given in the caption of the figure 9) is sufficient to describe the δ_θ and δ_U decreases with Ra over the three heat transfer regimes, once the spatial division (solid/fluid) is applied. The similarity between the smooth and solid BL, previously described for three particular Ra in figures 7 and 8, is confirmed. In the fluid zone, the decrease of both BL thicknesses (δ_θ and δ_U) is much slower, although it always remains larger than the BL thicknesses above the solid and smooth zones. However, it is noteworthy that the regime II begins with the crossing of δ_θ^{fluid} with H_p. This is in good agreement with previous experimental investigations made with different roughness shapes such as (Du & Tong 2000) using pyramids, (Tisserand *et al.* 2011; Salort *et al.* 2014; Xie & Xia 2017) using square based parallelepipeds or with the numerical study of Stringano *et al.* (2006) using grooved plates. Additionally, we observe that the regime II ends when δ_U^{fluid} becomes smaller than H_p, which was also observed experimentally (Xie & Xia 2017).

A second measure of the boundary layer thicknesses (noted δ^{rms}) considers the distance from the wall to the peak of the temperature or horizontal velocity rms-fluctuations. The figure 10 illustrates their evolution with Ra. Once again, we divide the rough cavity part into two parts, the *solid* zone above the roughness blocks and the *fluid* zone above the valleys. As already observed, the *smooth* and *solid* δ_θ^{rms} and δ_U^{rms} follow a similar trend, with a single scaling law describing the BL thickness decrease whatever the regime. We note that the thermal BL along the smooth wall remains always slightly thicker than the solid one above the roughness blocks. The fluid BL behaves in a different way. After becoming thinner with Ra in the regime I and II, δ_θ^{rms} and δ_U^{rms} tend towards a plateau

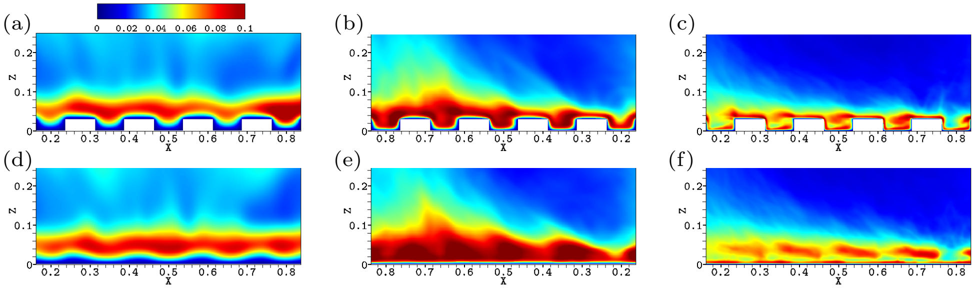

FIGURE 11. Temperature fluctuation rms field (θ_{rms}) on vertical planes in the vicinity of the rough plate for three particular Ra: (a,d) $Ra = 2 \cdot 10^6$ (regime I) ; (b,e) $Ra = 5 \cdot 10^7$ (regime II) ; (c,f) $Ra = 10^9$ (regime III). (a,b,c) between two rows of roughness blocks $y = 0.3125$; (d,e,f) at mid-depth of the cavity $y = 0.25$).

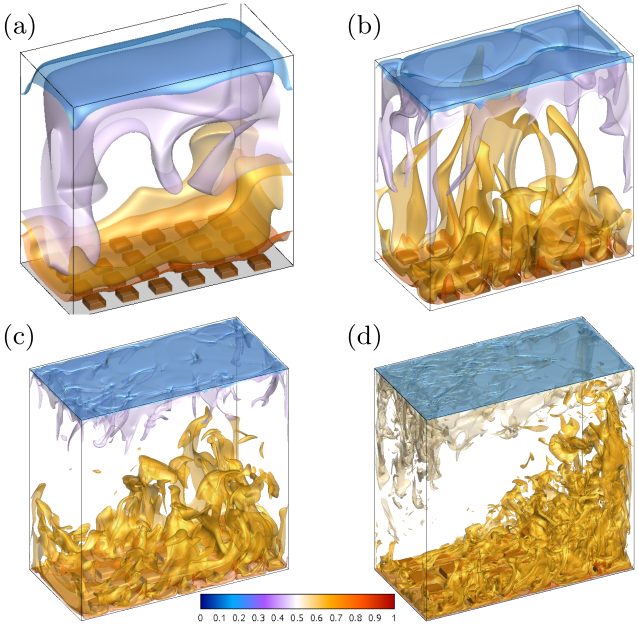

FIGURE 12. Instantaneous temperature field for (a) $Ra = 2 \cdot 10^6$ (regime I), (b) $Ra = 5 \cdot 10^7$ (regime II), (c) $Ra = 10^9$ (regime III) and (d) $Ra = 10^{10}$ (regime III). Isosurface values correspond to $\theta = (\ 0.2,\ 0.45,\ 0.65,\ 0.8)$.

in the regime III, that corresponds approximately to the roughness height. This plateau can be interpreted as the signature of a fluctuating rough fluid layer mentioned in the section 4.2. Moreover, for this regime and the fluid region, a second local maxima can be determined in the vertical profiles of temperature and velocity field *rms*-fluctuations, that defines a turbulent BL within valleys of a similar thickness to δ_θ^{rms} and δ_U^{rms} for the solid region and the smooth plate. It confirms the onset of a turbulent RB convection-like flow within valleys in the regime III.

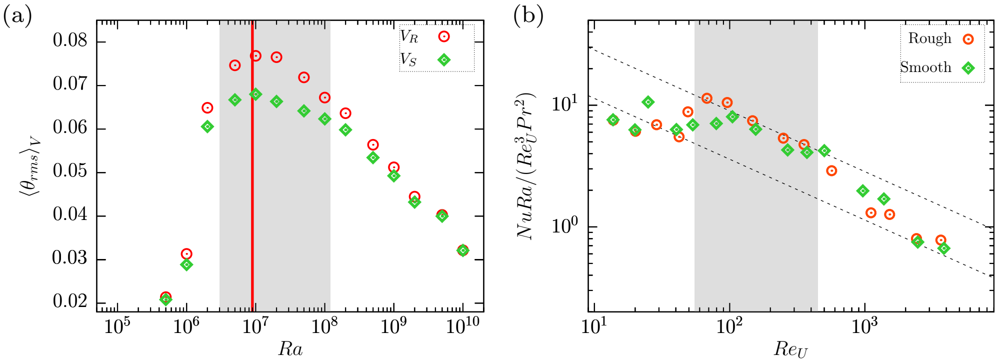

FIGURE 13. (a) Integral of rms temperature fields over the fluid volume in half a cavity (V_R volume of the rough half cavity ; V_S volume of the smooth half cavity). The vertical red line represents the critical Rayleigh number Ra_c. (b) Friction coefficient normalized by dissipation vs Reynolds number. The dashed lines display $Re_U^{-0.5}$ power laws. The shaded area illustrates the $Ra-$range of the regime II.

5.2. *Global flow structure*

The effect of roughness on flow structure is first investigated by considering temperature fluctuations around roughness (see figure 11). We observe that a turbulent layer develops around roughness in all cases. But, while in the regime I, this layer remains mainly above roughness, it fills almost entirely the valleys in the regime II. In the regime III, a less fluctuating small flow takes place within the valleys, with a BL along the bottom plate and a turbulent layer around $z \sim H_p$, illustrating interactions between the valley flow and the large scale circulation (LSC). These two layers are responsible of the two peaks observed in the rms-fluctuations used to define the BL thicknesses displayed in figure 10. Additionally, it is noticeable that the temperature fluctuations are particularly intense in the regime II, when comparing with regimes I and III.

The figure 12 illustrates how the change in the heat transfer regime modifies plume organization. A qualitative overview of the iso-contours of instantaneous temperature shows a number of large hot plumes within the cavity bulk in the regime II (figure 12-b), while plumes appear more altered by the LSC in the regime III (figures 12-c,d). Moreover, the asymmetry of the flow seems to appear for regimes II and III.

A more global point of view can be obtained by considering the spatial average of rms temperature over the volume of half a cavity ($V = V_R$ or V_S), as a function of Ra. As plotted in figure 13-a, the asymmetry of temperature rms-fluctuations only occurs in regime II, where larger values are present on the rough part of the cavity rather than on the smooth part. But for each half cavity, the maximum value of fluctuations is reached around Ra_c. Unlike regime II, the intensity of θ_{rms} is similar on both parts of the cavity in regimes I and III. These observations are in agreement with the statement of Du & Tong (1998), that interactions between roughness and LSC enhances the detachment of the thermal boundary layer leading to extra thermal plumes, but only in the regime II in our case.

Mechanical interactions of the LSC with roughness can be quantified considering the friction coefficient expressed as $NuRa/(Re_U^3 Pr^2)$, as suggested by Chavanne *et al.* (2001). The figure 13-b presents its evolution as a function of Re_U, that is the Reynolds number based on the maximum of the horizontal velocity ($\langle\overline{U}\rangle$). In a similar manner as Nu and Ra, Re_U can be estimated separately for the rough or smooth parts of the cavity. It is seen that the friction coefficient fits well with the expected $Re^{-1/2}$ power law, but surprisingly with a higher prefactor during the regime II by comparing with regime I and III. For very large Ra ($\geqslant 5 \cdot 10^9$), the friction coefficient tends to revert to the scaling law of the regime I. This can be interpreted as stronger interactions between the flow coming from the roughness region and the LSC, when the block top is sandwiched between the thermal and kinetic BL ($\delta_\theta \leqslant H_p \leqslant \delta_U$).

6. Conclusion

In this paper, we present DNS results of turbulent Rayleigh-Bénard convection in an asymmetric rough water-filled cavity for five decades in Rayleigh number ($Ra \in [10^5 - 10^{10}]$). The study case has been dimensioned in order to obtain a moderate value of the critical roughness-height-based Rayleigh number ($Ra_c = 9 \cdot 10^6$). The main objective is to determine whether particular physical mechanisms in the block surroundings can explain the enhanced heat transfer in regimes II and III. To this purpose, it is proposed to use a single physical set-up to capture the two successive heat transfer regime transitions.

First, a global description of the heat transfer in the asymmetric cavity R/S is discussed. As expected, we have identified three successive regimes of heat transfer: (i) a thermally resistant regime I where the global Nusselt number ($Nu_{R/S}$) is reduced comparing with the heat transfer in a perfectly smooth cavity ($Nu_{S/S}$), (ii) a transitional regime II where the heat transfer is particularly intense, and (iii) a regime III in which the increase of $Nu_{R/S}$ is larger than the relative increase of surface due to roughness. When the smooth and rough plates are separated, only one scaling exponent can describe the heat transfer on the smooth plate, whereas two scaling exponents stand for the rough plate ($Nu_R \sim Ra_R^\beta$): in regimes I and III, $\beta_R \sim 1/3$ is found and it increases to $\beta_R = 0.42$ in regime II.

In order to highlight the role of the inner fluid retained within roughness valleys, the horizontal plane at the roughness height is divided into two parts, which enables to define two distinct heat transfer contributions: a first one coming from the solid top surface of roughness blocks, and a second one crossing the fluid interface between the cavity bulk and the inner fluid. Whatever the heat transfer regime, a unique scaling law for the heat transfer on the solid top surface is found. In contrast, the fluid interface appears to drive the complete heat transfer along the rough plate (Nu_R). Concerning $Nu_R|_{H_p}^{fluid}$, the β exponent of the ($Nu - Ra$) scaling law is approximately $\beta_F \sim 1/3$ in regimes I and III and it increases to $\beta_F \sim 0.5$ in regime II.

By using the decomposition of the rough Nusselt number (Nu_R) into conductive and convective parts, it has been shown that conduction is the dominant heat transfer mode in regime I. Convection contribution becomes sufficiently large in regime II to compete against conduction. In regime III, convection becomes the dominant mode, while heat transfer by conduction saturates at a specific value. This value as well as the bulk temperature are shown to depend only on geometric parameters. It suggests that the flow in regime III is organized in the form of boundary layers flowing along the geometry of the top and bottom plates and of a separate fluctuating rough fluid layer overlaying roughness. The remainder of the fluid volume can be considered to be well mixed, including the small fluid volumes within the roughness valleys.

Since the heat transfer is initiated inside the boundary layers, the $Ra-$evolution of their thicknesses has been analysed by adopting the previous spatial division (viz. smooth plate / the solid zone above the top surface of blocks / the fluid zone located inside the valleys and above). Considering the displacement boundary layer thicknesses, the boundary layers above valleys are detected to mark out the limits of the regime II. As proposed by Xie & Xia (2017), this regime starts when the thermal boundary layer is thinner than the roughness height and ends when the kinetic boundary layer is thinner than the roughness height. Concurrently, the boundary layer above blocks behaves like the smooth boundary layer, becoming thinner than the roughness height early in the regime I. A measure of the fluctuating rough fluid layer thickness has been obtained by tracking the peaks of temperature *rms*-fluctuations. This measure points out the presence of this fluid layer only in the regime III.

Finally, as could be seen by adopting a global point of view, the top and bottom half-cavities display the same level of thermal fluctuations, except in regime II where more intense fluctuations are present in the rough part. This is in agreement with the Du & Tong (1998) interpretation of extra plumes emissions by roughness, but only for the regime II. More surprisingly, the global friction coefficient increases in both half-cavities during regime II, suggesting larger interactions between roughness and large scale circulation.

However, these conclusions pertain to a range of moderate Rayleigh numbers due to the value of the set critical Rayleigh number. Further investigations should be performed to clarify the interplays between roughness, large scale circulation and higher turbulence level.

7. Acknowledgments

This study was granted access to the HPC resources of GENCI-IDRIS under allocation 2a0326 made by GENCI. This work has benefited from the financial support of the INSIS CNRS (PEPS Energie 2018). We are grateful to Francesca Chillà and Julien Salort for valuable discussions.

REFERENCES

Ahlers, G., Grossmann, S. & Lohse, D. 2009 Heat transfer and large scale dynamics in turbulent Rayleigh-Bénard convection. *Rev. Mod. Phys.* **81**, 503–537.

Belkadi, M., Guislain, L., Sergent, A., Podvin, B., Chillà, F. & Salort, J. 2020 Experimental and numerical shadowgraph in turbulent Rayleigh-bénard convection with a rough boundary: investigation of plumes. *J. Fluid Mech.* **895**, A7.

Castaing, B., Gunaratne, G., Heslot, F., Kadanoff, L., Libchaber, A, Thomae, S., Wu, X.-Z., Zaleski, S. & Zanetti, G. 1989 Scaling of hard thermal turbulence in Rayleigh-Bénard convection. *J. Fluid. Mech* **204**.

Chavanne, X., Chillà, F., Chabaud, B., Castaing, B. & Hébral, B. 2001 Turbulent Rayleigh-Bénard convection in gaseous and liquid He. *Phys. Fluids* **13**.

Chillà, F. & Schumacher, J. 2012 New perspectives in turbulent Rayleigh-Bénard convection. *Eur. Phys. J. E* **35**, 58.

Derebail Muralidhar, S., Podvin, B., Mathelin, L. & Fraigneau, Y. 2019 Spatio-temporal proper orthogonal decomposition of turbulent channel flow. *J. Fluid Mech* **864**, 614639.

Du, Y.-B. & Tong, P. 1998 Enhanced heat transport in turbulent convection over a rough surface. *Phys. Rev. Lett.* **81**, 987–990.

Du, Y.-B. & Tong, P. 2000 Turbulent thermal convection in a cell with ordered rough boundaries. *J. Fluid Mech.* **407**, 57–84.

Emran, M. S. & Shishkina, O. 2020 Natural convection in cylindrical containers with isothermal ring-shaped obstacles. *J fluid Mech* **882** (A3).

Goda, K. 1979 A multistep technique with implicit difference schemes for calculating two- or three-dimensional cavity flows. *J. Comp. Physics* **30** (1), 76 – 95.

Grossmann, S. & Lohse, D. 2000 Scaling in thermal convection: a unifying theory. *J. Fluid Mech.* **407**, 27–56.

Grossmann, S. & Lohse, D. 2001 Thermal convection for large Prandtl numbers. *Phys. Rev. Lett.* **86**, 3316–3319.

Guermond, J.L., Minev, P. & Shen, Jie 2006 An overview of projection methods for incompressible flows. *Comp. Meth. Appl. Mech. Eng.* **195** (44), 6011 – 6045.

Hireche, O., Ramadan, I., Weisman, C., Bailliet, H., Fraigneau, Y., Baltean-Carls, D. & Daru, V. 2020 Experimental and numerical investigation of natural convection flows in two horizontal thermoacoustic cavities. *Int. J. Heat Mass transf.* **149**, 119195.

Jiang, H., Zhu, X., Mathai, V., Verzicco, R., Lohse, D. & Sun, C. 2018 Controlling heat transport and flow structures in thermal turbulence using ratchet surfaces. *Phys. Rev Lett* **120**, 044501.

Kaczorowski, M., Chong, K.L. & Xia, K.Q. 2014 Turbulent flow in the bulk of Rayleigh-Bénard convection: aspect-ratio dependence of the small-scale properties. *J. Fluid Mech* **747**, 73–102.

Liot, O., Ehlinger, Q., Rusaouën, E., Coudarchet, T., Salort, Julien & Chillà, F. 2017 Velocity fluctuations and boundary layer structure in a rough Rayleigh-Bénard cell filled with water. *Phys. Rev. Fluids* **2**, 044605.

Qiu, X.-L., Xia, K.-Q. & Tong, P. 2005 Experimental study of velocity boundary layer near a rough conducting surface in turbulent natural convection. *Journal of Turbulence* **6**, 30.

Roche, P., Castaing, B, chabaud, B. & Hébral, B. 2001 Observation of the 1/2 power law in Rayleigh-Bénard convection. *Phys. Rev. E* **63**, 045303.

Rusaouën, E., Liot, O., Castaing, B., Salort, J. & Chillà, F. 2018 Thermal transfer in Rayleigh-Bénard cell with smooth or rough boundaries. *J. Fluid Mech.* **837**, 443–460.

Salort, J., Liot, O., Rusaouën, E., Seychelles, F., Tisserand, J.-C., Creyssels, M., Castaing, B. & Chillà, F. 2014 Thermal boundary layer near roughnesses in turbulent Rayleigh-Bénard convection: Flow structure and multistability. *Phys. Fluids* **26** (1), 015112.

Stevens, R. J. A. M., van der Poel, Erwin P., Grossmann, S. & Lohse, D. 2013 The unifying theory of scaling in thermal convection: the updated prefactors. *J. Fluid Mech.* **730**, 295–308.

Stevens, R. J. A. M., Verzicco, R. & Lohse, D. 2010 Radial boundary layer structure and nusselt number in Rayleigh-Bénard convection. *J. Fluid Mech.* **643**, 495–507.

Strang, G. 2007 *Computational Science and Engineering*. Wellesley-Cambridge Press.

Stringano, G., Pascazio, G. & Verzicco, R. 2006 Turbulent thermal convection over grooved plates. *J. Fluid Mech.* **557**, 307–336.

Tisserand, J.-C., Creyssels, M., Gasteuil, Y., Pabiou, H., Gibert, M., Castaing, B. & Chillà, F. 2011 Comparison between rough and smooth plates within the same Rayleigh-Bénard cell. *Phys. Fluids* **23** (1), 015105.

Toppaladoddi, S., Succi, S. & Wettlaufer, J.S. 2015 Tailoring boundary geometry to optimize heat transport in turbulent convection. *EPL (Europhysics Letters)* **111** (4), 44005.

Toppaladoddi, S., Succi, S. & Wettlaufer, J.S. 2017 Roughness as a route to the ultimate regime of thermal convection. *Phys. Rev. Lett.* **118**, 074503.

Tummers, M.J. & Steunebrink, M. 2019 Effect of surface roughness on heat transfer in Rayleigh-Bénard convection. *Int. J. Heat Mass transf.* **139**, 1056 – 1064.

Wagner, S. & Shishkina, O. 2015 Heat flux enhancement by regular surface roughness in turbulent thermal convection. *J. Fluid Mech.* **763**, 109–135.

Wei, P., Chan, T.S., Ni, R., Zhao, X.Z. & Xia, K.Q. 2014 Heat transport properties of plates with smooth and rough surfaces in turbulent thermal convection. *J. Fluid Mech.* **740**, 28–46.

Xia, K.-Q. 2019 Tuning heat transport via boundary layer topographies. *J. Fluid Mech.* **876**, 1–4.

Xie, Y.C. & Xia, K.Q. 2017 Turbulent thermal convection over rough plates with varying roughness geometries. *J. Fluid Mech.* **825**, 573–599.

Yang, W., Delbende, I., Fraigneau, Y. & Martin Witkowski, L. 2020 Large axisymmetric surface deformation and dewetting in the flow above a rotating disk in a cylindrical tank: Spin-up and permanent regimes **5** (4), 044801.

Zhang, Y.Z., Sun, C., Bao, Y. & Zhou, Q. 2018 How surface roughness reduces heat transport for small roughness heights in turbulent Rayleigh-Bénard convection. *J. Fluid Mech.* **836**, R2.

Zhu, X., Stevens, R. J. A. M., Shishkina, O., Verzicco, R. & Lohse, D. 2019 $Nu \sim Ra^{1/2}$ scaling enabled by multiscale wall roughness in Rayleigh-Bénard turbulence. *J. Fluid Mech.* **869**, R4.

Zhu, X., Stevens, R. J. A. M., Verzicco, R. & Lohse, D. 2017 Roughness-facilitated local 1/2 scaling does not imply the onset of the ultimate regime of thermal convection. *Phys. Rev. Lett.* **119**, 154501.